

**Pore formation during dehydration of a polycrystalline gypsum sample  
observed and quantified in a time-series synchrotron X-ray micro-  
tomography experiment**

F. Füsseis<sup>1\*</sup>, C. Schrank<sup>2</sup>, J. Liu<sup>3,4</sup>, A. Karrech<sup>4,5</sup>, S. Llana-Fúnez<sup>6</sup>, X. Xiao<sup>7</sup>, K.  
Regenauer-Lieb<sup>3,4,8</sup>

<sup>1</sup> Institut für Geologie, Mineralogie und Geophysik, Ruhr-Universität Bochum,  
Germany

<sup>2</sup> School of Earth, Environmental and Biological Sciences, Queensland University  
of Technology, Brisbane, Australia

<sup>3</sup> Western Australian Geothermal Centre of Excellence, Perth, Australia

<sup>4</sup> CSIRO Earth Science and Resource Engineering, Kensington, Australia

<sup>5</sup> School of Mechanical Engineering, University of Western Australia, Crawley,  
Australia

<sup>6</sup> Departamento de Geología, Universidad de Oviedo, Oviedo, Spain

<sup>7</sup> Advanced Photon Source, Argonne, USA

<sup>8</sup> School of Earth and Environment, University of Western Australia, Crawley,  
Australia

\* corresponding author: [florian@fusseis.at](mailto:florian@fusseis.at)

**Abstract**

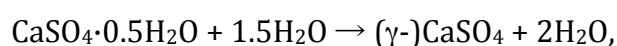
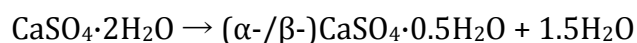
We conducted an in-situ X-ray micro-computed tomography heating experiment at the Advanced Photon Source (USA) to dehydrate an unconfined 2.3 mm diameter cylinder of Volterra Gypsum. We used a purpose-built X-ray transparent furnace to heat the sample to 388 K for a total of 310 minutes to acquire a three-dimensional time-series tomography dataset comprising nine time steps. The voxel size of 2.2  $\mu\text{m}^3$  proved sufficient to pinpoint reaction initiation and the organization of drainage architecture in space and time. We observed that dehydration commences across a narrow front, which propagates from the margins to the centre of the sample in more than four hours. The advance of this front can be fitted with a square-root function, implying that the initiation of the reaction in the sample can be described as a diffusion process.

Novel parallelized computer codes allow quantifying the geometry of the porosity and the drainage architecture from the very large tomographic datasets (2048<sup>3</sup> voxels) in unprecedented detail. We determined position, volume, shape and orientation of each resolvable pore and tracked these properties over the duration of the experiment. We found that the pore-size distribution follows a power law. Pores tend to be anisotropic but rarely crack-shaped and have a

preferred orientation, likely controlled by a pre-existing fabric in the sample. With on-going dehydration, pores coalesce into a single interconnected pore cluster that is connected to the surface of the sample cylinder and provides an effective drainage pathway. Our observations can be summarized in a model in which gypsum is stabilized by thermal expansion stresses and locally increased pore fluid pressures until the dehydration front approaches to within about 100  $\mu\text{m}$ . Then, the internal stresses are released and dehydration happens efficiently, resulting in new pore space. Pressure release, the production of pores and the advance of the front are coupled in a feedback loop.

## 1. Introduction

Since Heard and Rubey (1966) associated the dehydration of gypsum with a significant strength drop of the material, the reaction is often considered a model for the processes related to prograde devolatilization in tectonics and metamorphic geology. A wealth of studies was conducted to understand the mineralogy of the apparently simple reaction, but despite great efforts over the last hundred years or so, Charola et al. (2007), in their review of gypsum deterioration, had to point out that “a comprehensive approach to understand the true nature and behaviour of this ubiquitous compound [...] is still missing”. There seems to be consensus that the dehydration of gypsum is a two-step process:



in which gypsum, upon heating to temperatures larger than  $\sim 373\text{ K}$  first dehydrates into the metastable hemi-hydrate, which then dehydrates into  $\gamma$ -anhydrite (Bezou et al., 1995, Singh and Middendorf, 2007, Christensen et al., 2008, Jacques et al., 2009). The existence of a subhydrate  $\text{CaSO}_4 \cdot x\text{H}_2\text{O}$  has been discussed for some time, and recently Schmidt et al., (2011) proved that hemihydrate reacts to  $\text{CaSO}_4 \cdot 0.625\text{H}_2\text{O}$  in moist conditions. The dehydration of gypsum is an anomalously slow process compared to the dehydration of other compounds containing crystal water (Charola et al., 2007).

This paper focuses on the initiation of dehydration at  $388\text{ K}$ . At the temperature and time scales of our experiment, hemihydrate is expected to be the most common dehydration product (Freyer and Voigt, 2009). Two hemi-hydrate varieties are distinguished on the basis of their specific surface area, crystal sizes, habit and surface topography of the crystals (Freyer and Voigt, 2003, 2009, Singh and Middendorf, 2007). Where the dehydration reaction occurs under a

high partial water vapor pressure in acidic solutions,  $\alpha$ -hemi-hydrate forms.  $\beta$ -hemi-hydrate results from dehydration under dry conditions or in vacuum. By comparison, Hildyard et al. (2011) identified euhedral hemi-hydrate crystals in polycrystalline gypsum samples that were dehydrated at low confining and effective pressures as  $\alpha$ -hemi-hydrate (their experiments GYP37 and 38). The hemi-hydrate grains formed inequigranular, decussate aggregates.

Several models have been proposed as to how the reaction would progress in a polycrystalline sample (Olgaard et al., 1995, Ko et al., 1997, Miller et al., 2003, Wang and Wong, 2003). The model of Olgaard et al. (1995), refined in Ko et al. (1997), is probably based on the largest experimental dataset. Interpreting syn-experimental fluid expulsion measurements and micrographs made post-experimentally, they predicted dehydration to advance in three stages: a first stage, where the reaction commences throughout the sample but the released fluid is trapped in isolated pores, thus leading to high pore fluid pressures. In a second stage these pores are thought to interconnect and form a permeable network while fluid expulsion increases strongly. In a third stage, fluid expulsion decreases and the reaction comes to completion. Wang and Wong (2003) investigate this model numerically. They predict that dehydration occurs at a reaction front that propagates across a 25mm long sample in less than 200 minutes. Porosity increases smoothly across the entire length of the sample. Even though Wang and Wong duplicate the fluid-expulsion curves of Ko et al. (1997) quite accurately, their results contrast with earlier descriptions of very sharp reaction fronts in dehydrating gypsum specimens by Stretton (1996). In her Plate 11.1, Stretton shows a partly reacted sample where the dehydration initiates across a narrow zone less than 50  $\mu\text{m}$  wide.

Because the fluid volume ( $V_{\text{fluid}}$ ) increases slightly more than the solid volume ( $V_{\text{solid}}$ ) decreases during the reaction ( $|\Delta V_{\text{fluid}}/\Delta V_{\text{solid}}|=1.23$ ), pore fluid pressure is considered critical for the reaction progress, the formation of drainage pathways and fluid escape (e.g., Heard and Rubey, 1966, Murrell and Ismail, 1976, Ko et al., 1997, Llana-Fúnez et al., submitted). Miller et al. (2003) propose a model where hydraulic fracturing resulting from fluid overpressure exclusively controls drainage. Applying Hacker's (1997) classification, the dehydration reaction is fluid-dominated and driven by a decreasing pore fluid pressure. Llana-Fúnez et al. (submitted) associate fluid expulsion with reaction progress and show that a decreasing pore fluid pressure accelerates the reaction. It is known that the reaction is strongly pressure sensitive (McConnel et al., 1987, Karrech et al., in prep.) and only proceeds where pore fluid pressures are

relieved by water draining from the reaction site (Miller et al., 2003, Llana-Fúnez et al., submitted). This renders the formation of permeable porosity critical for the reaction progress (Olgaard et al., 1995) and a hinge for all models of dehydration of polycrystalline gypsum.

All current models for dehydration of polycrystalline gypsum under drained conditions are based on the indirect assessment of reaction progress and porosity formation through fluid expulsion and the post-experimental, two-dimensional analysis of reaction fabrics in samples reacted to different extents. These are obvious limitations that were acknowledged by previous authors (Ko et al., 1997, Wang and Wong, 2003).

Here we apply a novel workflow that allows documenting the reaction progress in situ in three dimensions with high temporal and spatial resolution. We conducted a drained heating experiment in an X-ray transparent furnace and monitored reaction progress with synchrotron radiation based X-ray micro-computed tomography to acquire a volumetric time-series data set of the porosity evolution during dehydration. By documenting all pores larger than  $2.2\mu\text{m}^3$  in volume, the tomographic time series data allow to precisely document the reaction. We quantify the progress of the dehydration front and analyse the organization of the drainage architecture in space and time.

## **2. Materials and methods**

### **2.1 Volterra Gypsum**

We cored a 2.3 by 8 mm cylinder from a block of Alabaster from Volterra, Italy. This polycrystalline material has become a standard for gypsum dehydration experiments (e.g., Ko et al., 1995, Olgaard et al., 1995, Miller et al., 2003, Llana-Fúnez et al., submitted). Stretton (1996) determined a mean grain size of 120  $\mu\text{m}$  using a line intercept method on thin sections.

We used the intercept software of Launeau et al. (2010) to determine mean grain size and to analyse shape anisotropy in both secondary electron images taken from polished sections and photographs of thin sections acquired under polarized light and with crossed polarisers. The mean grain size of Volterra gypsum is between 45 and 123  $\mu\text{m}$  (Table 2). Using this grain size interval, we estimate that the imaged part of our sample contains between 10,000 and 60,000 grains. Thin sections reveal that the material can be fairly heterogeneous locally (Suppl. Figure 1). The aspect ratios of shape-fabric ellipsoids range from 1.09 to 1.52, indicating local shape-preferred orientations. Pockets of platy high-

aspect ratio gypsum crystals were found to cover areas of a few square millimetres in size (Suppl. Figure 1). We have no indication that our tomographic sample is composed of grains of this size.

## **2.2 Synchrotron Tomography**

We used synchrotron radiation based X-ray micro-computed tomography (SR $\mu$ CT) to document the progress of gypsum dehydration in 3 dimensions. SR $\mu$ CT is based on two-dimensional digital radiographs that record the attenuation of coherent X-rays penetrating a sample. The attenuation of X-rays is a material property related to density; hence in compositionally heterogeneous samples the recorded X-ray absorption varies spatially. Radiographs shot from changing viewpoints are combined, using reconstruction algorithms, in a three-dimensional model of the distribution of different materials in a specimen (e.g. Stock, 2009), in our case gypsum, hemi-hydrate and pores. During reconstruction, the spectrum of absorption values recorded in a sample is mapped into a 32-bit gray value space ( $2^{32}$  gray levels mapped into the numeric interval from -0.008 to 0.008). Several tomographic datasets acquired at different points in time from the same dehydrating polycrystalline gypsum sample can be merged in a four-dimensional (i.e. a time series) dataset.

Microtomographic data were collected at the bending magnet beam line 2-BM at the Advanced Photon Source, Argonne National Laboratory, USA. A double multilayer monochromator of 1.5 % bandwidth provided 27 KeV X-rays; images were collected in transmission mode by a CCD camera behind the sample in the hutch configuration. Data were collected through rotating the samples in steps of  $0.125^\circ$  over  $180^\circ$ . The acquisition time for each data set was about 25 minutes, which allowed for nine scans during the experimental run.

## **2.3 In-situ heating experiment**

For the experiment, we used an X-ray transparent furnace that was installed within the tomographic setup (Figure 1). The furnace consists of a hollow cylinder, made from  $\text{Al}_2\text{O}_3$  ceramic, 10\*30 mm in dimension, with a lid to limit the heat loss. The wall thickness of the cylinder is 1.5 mm. X-rays are allowed to penetrate the sample through two uncovered rectangular windows (4x4 mm) 3 mm from the bottom edge of the furnace. Two heating wires, coiled around the cylinder above and below the windows, heat the furnace. The sample, which was glued to a 25x25x13 mm Al-Si ceramic block at its base, was inserted into the furnace from the bottom. The ceramic base block insulated the rotation stage from the heat above. We rotated the entire lower assembly, which included the

stage, the base block and the sample, for data acquisition. A thermocouple was mounted to the base of the sample cylinder. For all glued connections (heating coil and sample mounting, thermocouple installation) we used high-temperature Sauereisen No. 7 cement.

We heated the sample to 388 K for a total of 310 minutes (Suppl. Figure 2). The experiment began with short heating periods (1, 2, 3 and 4 minutes), followed by five heating periods of 60 minutes each. In between each heating period, the reaction had to be suspended for data acquisition, and the sample was passively cooled to 323 K in about 2-3 minutes (Suppl. Figure 2). After each scan, the furnace was heated to reaction temperatures in 46 s (ramp rate  $150^{\circ} \text{ min}^{-1}$ ). The experiment yielded a total of nine datasets (i.e. time steps). Before and after data acquisition, the sample experiences temperature fluctuations of 65 K that propagate through the cylinder. The time it takes for the sample to equilibrate thermally after each scan can be calculated from the thermal diffusivity and the dimension of the sample (Clauser and Huenges, 1995, Regenauer-Lieb and Yuen, 2004):  $t = 4 r^2 / D_T$ , where  $t$  is the time scale,  $r$  is the sample radius and  $D_T$  is the thermal diffusivity. For a thermal diffusivity of gypsum of  $0.285 \times 10^{-6} \text{ m}^2 \text{ s}^{-1}$  (Clauser and Huenges, 1995) and a sample radius of 1.3 mm this indicates thermal equilibration in less than 20 seconds. This allows us to conclude that diffusion of heat (i.e., a thermal gradient) does not influence the kinetics of the reaction in our sample. All times given in the further text are *minutes at 388 K*, the reaction temperature.

A dummy sample was employed to train a *Eurotherm 2404* controller to heat the specimen with a precision of about  $1^{\circ}$ . Only one thermocouple was used in the experiment, and we have no information on the temperature distribution in the furnace. While air was certainly circulating through the openings in the furnace we believe that the very responsive heater and the small dimension of the sample prevented major temperature gradients across the sample.

Gypsum dehydration has been studied in numerous experiments under a large range of boundary conditions and excellent reproducibility of experiments was demonstrated. Given the significant costs and efforts that it took to conduct the experiment reported here, we restrict ourselves to a single sample specimen. We are confident that our principal findings can be reproduced.

## 2.4 Data processing and analysis

Three-dimensional models were reconstructed from 1440 tomographic

projections/time step for all nine time steps of this study using Advanced Photon Source in-house algorithms and facilities. Each projection image comprises 2048x1536 pixels in raw format and each reconstructed three-dimensional dataset is discretized into a stack of 1536 horizontal image slices with a vertical spacing of 1.3  $\mu\text{m}$ . During 3D rendering, these image slices are combined in a volumetric dataset consisting of 2048x2048x1536 voxel. The minimum effective pixel size achieved was 1.3  $\mu\text{m}$ , yielding a volume of 2.2  $\mu\text{m}^3$  per voxel. All of our datasets proved of excellent quality, with a minimum of noise and artefacts. The data document a 2 mm section out of the upper half of the specimen cylinder, just above the thermocouple; the top of the cylinder is not included in the dataset.

The X-ray absorption of gypsum and hemi-hydrate proved sufficiently different from water and air to clearly distinguish pores from minerals, and the achieved spatial resolution is sufficient to do so (Figure 2). It is difficult to distinguish Gypsum and hemi-hydrate in the reacted part of the sample.

We use the term *pore* for any void space irrespective of the shape and size (cf. Sprunt and Brace, 1974). Due to their low X-ray attenuation, pores occupy the low end of the grey value histogram derived from a tomographic dataset (Figure 3). We segmented pores from solids by binary thresholding. The process, which requires the determination of a critical threshold, separates all voxels into those that belong to pores and those that do not.

For binary thresholding, determining the correct threshold value is critical (Kaestner et al., 2008 and references therein). In our case the reaction affects the grey value distribution and we found that we could use these changes to accurately determine the threshold value (Figure 3). For all time steps, we calculated histograms of the grey value frequency distribution from 180 million voxels that constitute a parallelepiped just off the centre of the sample cylinder (400x600x750 voxel<sup>3</sup> or 520x780x975  $\mu\text{m}^3$ ). As the reaction proceeded through the parallelepiped, hemihydrate and pores formed, and consequently voxels were reassigned amongst the 1024 bins constituting the histogram. Hemihydrate is denser than gypsum; therefore voxels that were gypsum and become hemihydrate assume a grey-value greater than that of gypsum. In the histogram, these voxels will increase the 'height' of the bright right shoulder (Figure 3). On the other hand, pores, water- or gas-filled have a much lower density than gypsum and hemihydrate. Therefore, voxels that were gypsum and turned into pores will attain grey values smaller/darker than that of gypsum and

hemihydrate. They will increase the frequency of dark voxels and hence contribute to the dark left shoulder of the histogram (Figure 3). This low-absorption shoulder is delimited by an intersection point of all histograms at a grey value of 0.00018 (inset in Figure 3), which separates the brighter bins occupied by gypsum voxels from darker bins of pore voxels. We used this value to segment pores from gypsum and hemihydrate in all datasets.

All pores in the above-mentioned parallelepiped were analysed. We use the method of Liu et al. (2009) to label face-connected clusters of 'porous' voxels as individual pores. We calculate the position, volume, surface, shape and orientation of each individual pore. In the datasets obtained after prior to heating and 10, 70, 130, 190, 250 and 310 minutes at reaction temperature, we determined frequency distributions for pore size, pore shapes, pore orientation and performed a percolation analysis.

We furthermore used a moving window method to analyse the porosity increase along a radius of the sample in the dataset obtained after 10, 70 and 130 minutes. We migrated a 20x400x750 voxel large box along the x-axis across the dehydration front described below. The radius was chosen so that the front was crossed in sections with low curvature. We used a step size of 1 voxel, and quantified the porosity in each box. We ascribe the fact that, in this analysis, we recorded porosity values that exceed the theoretically expected 29 % to result from the narrow sampling box combined with a locally heterogeneous distribution of porosity.

Two error sources affect SR $\mu$ CT data: errors introduced during data acquisition and reconstruction (Banhart, 2008) and the common discretization error of raster data (e.g. Arns et al., 2002). We estimated the combined error conservatively by assuming that the surface of each pore is subject to an uncertainty of  $\pm$  one voxel with respect to the surface normal vector. Since the topology of pore space is very complex, we determined this error empirically by a numerical dilation/erosion experiment: we expanded and shrank each pore in the parallelepiped by one voxel on their outer faces (Liu & Regenauer-Lieb, 2011) and then quantified the respective changes in the data. Apart from returning error margins for our quantification, this test provides insight into the pore structure and we discuss the results below. We stress that these error margins significantly overestimate the true error.

The data were visualized using the imaging software Avizo Fire.



### 3. Results

The following chapter is subdivided into two parts: A first part (Subsection 3.1) describes the two textural domains we identified in the data and the dehydration front that separates them. We quantified the advance of this front in the sample over time to assess the reaction progress through dehydration initiation. In a second part (Subsection 3.2) we analyse the porosity evolution behind the dehydration front to characterize the drainage architecture in the sample and its evolution during the experiment.

#### 3.1 Dehydration initiation

The tomographic data acquired of the partly dehydrated sample reveal two textural domains, separated by a narrow boundary (Figure 2). The inner textural domain shows a relatively homogeneous X-ray absorption. Based on the histogram obtained from the unreacted sample (Figure 3) the attenuation pattern in the inner domain is attributable to gypsum. The outer textural domain shows a more heterogeneous and wider absorption distribution resulting from abundant porosity in between the (denser) solid phases, gypsum and hemihydrate (Figures 2). Over the course of our experiment the relative widths of these domains change and the narrow boundary separating them migrates steadily inwards from the periphery of the sample cylinder (Figure 2).

We use the porosity, which is indisputably a result of the reaction, as a proxy for the onset of dehydration. As only very few pores were documented in the inner domain (Figure 2), we infer that, on the scale that we could resolve in the tomographic datasets, gypsum is stable there. Consequently we interpret the advancing boundary between the inner and the outer textural domain as a dehydration front that delimits the gypsum stability field spatially. The front marks the point where, on the scale of observation, gypsum becomes unstable and dehydration advances rapidly. The dehydration front itself exhibits a steep porosity gradient (Figure 4). Porosity increases from between 2.7 and 6.8 % to about 30 % over a distance of 100 - 200  $\mu\text{m}$ . The gradient remains similar over the duration of the experiment.

We tracked the progress of the dehydration front in two horizontal and two vertical tomography slices at times 3, 6, 10, 70, 130 and 190 minutes (Figures 5a,b). We measured the cumulative radial propagation,  $r_\alpha(t)$ , of the dehydration front.  $r_\alpha(t)$  denotes the distance that the dehydration front has travelled over the time  $t$  from the sample margin along a radial line of orientation  $\alpha$  (Suppl. Figure

3). The long axis of the cylindrical sample is defined as Z-axis. Radii are defined as lines in the plane normal to Z that connect the sample margin and the centroid of the unreacted domain. In horizontal slices, we determined  $r_{\alpha}(t)$  in steps of  $0.5^{\circ}$  for the interval  $[0^{\circ}; 360^{\circ}]$  at a given height  $z_i$ . We chose horizontal slices located in the middle of the sample volume (at  $\sim Z/2$ ) to avoid early interference with the dehydration front propagating inward from the top surface of the sample. The vertical slices represent the XZ- and the YZ-plane of the sample, respectively, and cover the entire height of the imaged sample volume. Hence, the orientations of the considered radii are  $0^{\circ}$  and  $180^{\circ}$  for the XZ-plane and  $90^{\circ}$  and  $270^{\circ}$  for the YZ-plane (Suppl. Figure 3). In each vertical slice, radial progress was determined not only for two opposite orientations but also at different vertical positions. We used a vertical step size  $\Delta z$  of  $13 \mu\text{m}$  for each pair of measurements (Suppl. Figure 3). In addition, the temporal evolution of the proportion of dehydrating area with respect to total sample area was calculated for the horizontal slices (Suppl. Figure 4).

The results show that the dehydration front propagates in a non-linear fashion (Figure 5). It moves faster in the beginning of the experiment and slows down subsequently. There is a marked asymmetry in dehydration front progress. The front moves faster in the right side of the sample in the XY-plane (i.e., the clockwise orientation interval  $[270^{\circ}; 90^{\circ}]$ , Figure 5a). In other words, the centroid of the unreacted domain does not coincide with the centroid of the sample cylinder. We used a non-linear least squares method to fit the results with a linear diffusion function of the type

$$\overline{r_{\alpha}(t)} = \sqrt{Dt}, \quad [1]$$

where  $\overline{r_{\alpha}(t)}$  is mean distance of front to sample margin,  $D$  is a constant diffusivity, and  $t$  is time. We obtain a  $D$  of  $8.29 \times 10^{-11} \text{ m}^2\text{s}^{-1}$  with  $r^2 = 0.71$  if we fit Eq. 1 to all data (Figure 5c).

The initially smooth front exhibits a variable roughness with a trend to irregularities with higher amplitudes later during the experiment (Figures 2 and 5a). The wavelength of these front indentations, 20 to  $100 \mu\text{m}$ , is of the same order of magnitude as the mean grain size of the sample (cf. Table 1). None of the undulations persists beyond one hour. In cases, individual cusps become narrow plumes of  $\mu\text{m}$ -sized pores extending up to  $200 \mu\text{m}$  into unreacted gypsum. In three dimensions, these ‘plumes’ are irregular porous sheets that are usually directly connected to a large pore in the outer domain. In the very early stages of the experiment, we did observe an alignment of these plumes with some of the cracks described below. The plumes occasionally surround volumes that are left

behind by the moving dehydration front. In these volumes, porosity increases with time.

Over the first three hours we found isolated crack-like features in the specimen. The width of these features is at the resolution limit, their longitudinal extent up to several hundred  $\mu\text{m}$ . They showed no preferred orientation. We did not see an increase in their number, or width, as the experiment progressed. Neither did we see any porosity associated with the features apart from a few very early pores following them at the periphery of the sample. Based on Stretton's (1996) and Milsch and Scholz's (2005) reports on the deformation microstructures developed in gypsum we are uncertain whether these features are cracks. As they did not affect the reaction progress we do not consider them any further.

## **3.2 The porosity and drainage architecture during dehydration**

### *3.2.1 Porosity*

Visual inspection of the porosity in the dehydrating domain indicates that the porosity consolidates rapidly once the front has passed (Suppl. Figure 4). We quantified the temporal evolution of porosity in the parallelepiped to better understand this consolidation and the geometry of the dehydration architecture. The porosity evolution is summarized in Table 2 and Figures 6 to 8.

The unreacted sample exhibits a porosity of 2.32 % (Figure 6a), which is somewhat higher than the previously published figures for Volterra gypsum (0.5 %, Ko, 1993, 0.1 %, Stretton, 1996) and probably related to different measurement techniques and minor local variations in porosity. As the reaction front propagates through the parallelepiped, the total porosity increases. After 130 minutes, when the front has propagated through the parallelepiped, the porosity peaks at 25.67 %. The porosity then decreases slightly to 24.01 % over the next three hours. Both values are remarkably close to the theoretically predicted 29% (e.g., Ko et al., 1997), which we consider an indication that the critical threshold used for segmentation of the data is appropriate.

The total number of pores is very high in the unreacted dataset (> 2.1 million, Figure 6b), increases at first as the dehydration front propagates into the sample (10 minutes) but then decreases to 0.53 million after 130 minutes. Over the next three hours it increases again to reach 0.63 million after 310 minutes, indicating that more pores accommodate slightly less porosity. The observed changes in total porosity and the number of pores once the front has passed (130 minutes) are subtle and within the discretization error. The datasets from the numerical

expansion/shrinking experiment essentially mirror this evolution of the total porosity, despite the obviously quite different absolute values (Figure 6a). Expansion reduces the total number of pores at all times, while shrinking increases them to a level above the original data after 130 minutes (Figure 6b). This indicates that pores formed during the reaction are not isometric, so that shrinking leads to a break up into several smaller pores. Furthermore it shows that they are close enough to each other so that expansion by just one voxel joins neighbouring pores.

The pores in the outer domain span a wide range of sizes, from one to a maximum of 43 million voxel. Porosity in the unreacted sample is comprised of a large number of very small pores (Figure 7); pores smaller than  $100 \mu\text{m}^3$  make up more than 95 % of the total porosity (Figure 8), with pores smaller than  $5 \mu\text{m}^3$  contributing more than 50 % of the porosity. The pore size frequency distribution evolves from the unreacted one until it assumes a characteristic shape and position after 130 minutes (Figure 7). After that, the changes are subtle but marked by an increase of especially the smallest pores (inset in Figure 8). While after 130 minutes the contribution of pores smaller  $1000 \mu\text{m}^3$  is only 6 % of the total porosity, the value increases to about 8 % after 310 minutes.

The dehydration-related porosity is characterized by the formation of one very large pore after 70 minutes (Figure 9). This topologically very complex pore accounts for more than 90 % of the total porosity (Table 2, Figure 8). It is four orders of magnitude larger than the second largest pore, intersects all faces of the parallelepiped and seems responsible for drainage of the volume. A visualization of this pore in a horizontal cross section shows that it connects the sample margin with the reaction front (Suppl. Figure 4).

As indicated by the shrinking test, the pores formed during dehydration are not isometric and this does not change over the course of the experiment. We characterize the shape of a pore by its isotropy index ( $i_i$ ), which is defined as  $i_i = e_3/e_1$ , with  $e_1$  and  $e_3$  being the largest and smallest eigenvalue, respectively, of the orientation matrix of a pore as defined in Liu et al. (2009).  $i_i = 1$  denotes an isotropic shape, while ‘cracks’ in the definition of Sprunt and Brace (1974) have  $i_i$  equal to or smaller than 0.1.

For this analysis we only consider pores larger than 50 voxel to minimise shape artefacts resulting from the limited possibilities to approximate the shape of small pores by a small number of (cubic) voxels. We also excluded pores larger

than 1200 voxel, as their shapes are too complex to be accurately described by the method (cf. Suppl. Figure 5). Our analysis shows that after 130 minutes 78 % of the pores have an isotropy index smaller than 0.5 but larger than 0.2 (Figure 10). There is a tendency for larger pores to being more anisotropic. After 130 minutes only 0.6 % of all pores have isotropy indices equal to or smaller 0.1. After 310 minutes, 0.4 % of pores have isotropy indices of 0.1 or smaller, whereas 80.1 % have isotropy indices between 0.2 and 0.5.

### 3.2.2 Drainage architecture

The grain shape analysis we conducted on Volterra alabaster indicated a slight shape-preferred orientation of grains (Table 1). To test the influence of such a pre-existing fabric on the evolving porosity, we determined the orientations of pores of three different size fractions (51-150 voxel, 151-300 voxel and 301-450 voxel) at different times during the experiment. The orientation of a pore is represented by azimuth and dip angle of  $e_1$  with respect to the coordinate system (Figure 2). Figure 11 illustrates the orientation of pores in the subsampled parallelepiped prior to heating, after 70 minutes and after 310 minutes. The orientations from the latter two datasets show the preferred alignment of pores along a great circle at an angle of about 30 degrees to the xz-plane, with a maximum close to the x-axis. Albeit weaker, due to the smaller number of pores, this trend can already be seen in the sample prior to heating (Figure 11a). In the datasets acquired during dehydration, pores of all three size-fractions follow this trend. The maximum density of  $e_1$  orientations of the smallest size fraction (expressed through the contour lines in Figure 11b and c) rotates, within the xy-plane, into the great circle between 70 and 310 minutes.

The cumulative pore size frequency distribution indicates that soon after the dehydration front has passed, pores interconnect. We conducted a percolation analysis to investigate this observation further. Percolation here refers to the connectivity of pores (Stauffer and Aharony, 1994). A moving window method was used (Liu et al., 2009), where cubes of various side lengths (25, 50, 100 and 200 voxel) are moved through the segmented datasets with a step size of 5 voxel. For each cube position the porosity in the cube and pore connectivity in the principal directions of the coordinate system are determined. For a given cube size, the analysis yields the porosity frequency distribution for all cube positions (Figure 12), as well as probability functions for percolation in the principal directions for all cube placements (Figure 13).

The porosity frequency distribution illustrates how homogeneously porosity is

distributed in the sampling volume (Figure 12). The more heterogeneously porosity is distributed, the wider the porosity frequency distribution will be. Vertical lines mark the total porosities measured in the parallelepiped (Table 2) for reference. The distributions of porosities amongst the cube placements for the datasets from 130 to 310 minutes are narrow and have their maxima within 2.5 % of the measured total porosities. The frequency distributions derived from the 10 min and 70 min datasets reflect a comparatively large variability amongst the cubes, which is due to the circumstance that the dehydration front is still propagating through the parallelepiped at these times.

The spatiotemporal ability of a volume to drain is controlled by the degree of interconnectivity of pore space. Probability functions for percolation in the three principal directions for each time step describe the time-dependent evolution of percolation in the parallelepiped. Each of the four diagrams in Figure 13 compares the probabilities for percolation in a 50x50x50 voxel cube with a given porosity for two successive time steps. It becomes evident that the differences between the probability functions for the three directions are subtle, particularly after 130 minutes, and cubes with a porosity of 20% or more are percolating in all three directions with a probability of more than 90%. However, cubes with porosities below ~19 % are more likely to percolate in the x-direction.

#### **4. Interpretation and discussion**

In-situ SR $\mu$ CT time-series experiments and their quantitative analysis provide a novel way of studying tectono-metamorphic processes, fluid-rock interaction and secondary porosity. Despite its comparatively simplistic setup, our experiment overcomes the 'black box' limitations of previous experimental studies and maps a way towards the discrete characterization of metamorphic dehydration. Our results provide detailed insight into the advance of dehydration in polycrystalline gypsum, the porosity-forming mechanism and the influence of pre-existing fabric anisotropy on drainage at atmospheric pressures.

##### **4.1 Dehydration initiation**

Confirming previous observations, our tomographic data show that the dehydration reaction propagates radially from the outer surface of the sample, where the water released during the reaction can escape, to the sample centre (Figure 2, e.g. Ko et al., 1997, Miller et al., 2003, Llana-Fúnez et al., 2007). A dehydration front delimits the drained portion of the sample (Figures 2, 4, 5) from an inner domain. In this inner domain no resolvable fluid drainage pathways are created and gypsum is essentially stable. The stability of gypsum

ahead of the dehydration front can be explained with the well-known pressure-dependence of the reaction. Karrech et al. (in prep.) recently revised experimental data by McConnell et al. (1987) and showed that, at 388 K, gypsum is stable at pressures of > 53 MPa. Karrech et al. (in prep.) demonstrate that the primary pressure source for reaction suppression in the sample interior derives from internal stresses due to the anisotropic thermal expansion of gypsum (cf. Ballirano and Melis, 2009).

We interpret the slightly increasing background porosity in the sample interior (Figure 4) to indicate that the reaction commences in the inner domain wherever water can drain into pre-existing pores or thermal cracks (Olgaard et al. 1995, Ko et al. 1997). As previously recognized, the resulting local increase in pore fluid pressure will help to suppress the reaction. However, our data also indicate that any pores that form ahead of the dehydration front remain largely below the resolution limit of about 1  $\mu\text{m}$ , and that they do not destabilize the slow advancement of the dehydration front. The reaction is suppressed until the dehydration front has approached.

We interpret that gypsum breakdown and pore formation are very efficient once the dehydration front has approached to within about 100  $\mu\text{m}$ , or roughly one average grain diameter. We postulate that the key processes during dehydration are intrinsically coupled in a feedback loop related to pressure changes across the dehydration front. At the dehydration front, the thermal-elastic internal and fluid-induced stresses are no longer in static equilibrium, and pore fluid that was previously trapped in pores is released into the drainage system. The resulting pressure drop drives the reaction, i.e. the dehydration of gypsum, which produces new pore space and consequently advances the dehydration front. This feedback operates on a grain-by-grain basis and controls the advancement rate of the dehydration front.

Our model for the dehydration of polycrystalline gypsum conflicts with an important aspect of the model by Olgaard et al., (1995) and Ko et al. (1997). Based on post-experimental observations from thin sections they interpret that the reaction products and their porous haloes grow to diameters of tens of  $\mu\text{m}$  *throughout the sample* before they interconnect and the fluid drains. In our three-dimensional data set we do not observe isolated nuclei of that size ahead of the dehydration front, and we therefore believe that Ko et al. possibly interpreted an oblique section through a very irregular but narrow reaction front.

An obvious difference between our and previous studies done with Volterra alabaster is the lacking confinement of our sample, which leaves it free to drain through most of its surface. Other investigators generally applied at least some confining pressure, limited drainage to one end of the cylinder and controlled the pore fluid pressure (Olgaard et al., 1995, Stretton, 1996, Ko et al., 1997, Miller et al., 2003, Llana-Fúnez et al., submitted). The drainage configuration certainly affects the overall geometry of the dehydration front in the sample, and both pressure sources control compaction in the outer domain and contribute to thermal-elastic internal stresses. However, our observations of a very narrow dehydration front with a steep porosity increase are strikingly similar to those made by Stretton (1996), who conducted her experiments under very similar conditions than Olgaard et al. (1995) and Ko et al., (1997). We interpret this to indicate that neither the drainage configuration nor a moderate confining pressure fundamentally change the breakdown behaviour of polycrystalline gypsum.

The dimensions of the dehydration front and the porosity evolution as observed in our data are in conflict with those modelled by Wang and Wong (2003). These authors postulate a smooth porosity increase of about 8% over a sample length of 25 mm (cf. their figure 7b). The reasons for this disparity remain to be clarified. In a companion paper (Karrech et al., in prep.), we develop a theory that captures the advance of the dehydration front on the basis of the dissipative mechanisms underlying the above feedback, and successfully reproduce both the sharp dehydration front and its progress over time.

In brief, this theory describes the advance of the reaction front as a pressure diffusion process, accounting for thermal-elastic internal and fluid-induced stresses in a coupled manner. The linear diffusion constant governing the advance of the dehydration front due to pressure diffusion can be derived from our experiment by fitting the front propagation data with Eq. 1 (Figure 5b). We obtain a value of  $8,290 \times 10^{-11} \text{ m}^2\text{s}^{-1}$  ( $r^2 = 0.71$ ). The spread of the data in Figure 5b is due to the undulations of the dehydration front and its asymmetric progress (Figures 2 and 5a). As discussed in the following section, both front undulations and asymmetric propagation are most likely a result of the lattice/fabric control of gypsum breakdown and porosity formation. The resulting data spread implies that our sample cannot be regarded as a homogeneous medium on the length scale of the sample radius. However, we calculated the percentage of reacted sample area in horizontal cross section over



time assuming a perfectly concentric reaction progress and using the diffusion constant obtained here and compared it to the percentage of reacted sample area determined in the physical experiment. Theoretical prediction and measured data match very well (Suppl. Figure 4). This might indicate that our small sample approaches statistical homogeneity with regards to microstructure at the scale of the entire sample cylinder. However, determining the representative elementary volume for Volterra alabaster is beyond the scope of this work. The diffusion constant determined here should therefore be understood as rough estimate with an uncertainty of plus/minus one order of magnitude (see also Figure Rose of Diffusivities). Nevertheless, it constitutes a material property than can be employed to predict the progress of the dehydration front in drained, unconfined gypsum.

#### **4.2 Gypsum breakdown and porosity formation**

We interpret the highly anisotropic gypsum lattice to control the actual breakdown process as well as the shapes of the pore nuclei in a similar way as it controls the formation of hemi-hydrate. Sipple et al. (2001) show that hemi-hydrate forms a pseudomorph after the parent gypsum crystal. Hildyard et al. (2011) observed the inheritance of a crystal preferred orientation in hemi-hydrate from parental gypsum and they employ Freyer and Voigt (2003), who predict a topotactic growth relationship between the two minerals. Finally, Finot et al. (1997) documented dehydration of gypsum in-situ and observed a remarkable mobility of water molecules along the (010) lattice planes, outlining preferred evacuation pathways that must have been provided by intracrystalline pores. Combining these observations, and considering the volume change that is involved in the formation of hemi-hydrate, it seems likely that pores that nucleate on the lattice scale follow the crystallographic orientation of their parental grains. We interpret our observation that the observed front irregularities (Figure 2) and the characteristic width of the dehydration front (Figure 4) are of similar size as the mean grain size (Table 1) as indirect evidence for the crystallographic control of dehydration at the grain scale.

We expect the orientation of gypsum grains to control the advance and organization of the dehydration front in a polymineralic gypsum rock (Figure 14). In volumes that exhibit a high degree of fabric anisotropy, which Volterra alabaster does on the millimetre scale according to our analysis (Suppl. Figure 1, Table 1), the dehydration should advance faster in the direction of the (010) lattice planes (Finot et al., 1997). We interpret our data to reflect such a pre-existing anisotropic fabric in parts of the sample: (1) the orientation of pre-

existing pores in the sample is highly anisotropic (Figure 11a), and new pores follow this orientation (Figure 11b, c); and (2) the progress of the dehydration front is highly asymmetric (Figure 5a, c). A pre-existing fabric would also align grain boundaries and thermal-elastic damage. We interpret the observed plumes to map such zones of enhanced drainage. An alternative possibility to explain the anisotropy would be heat loss through the thermocouple and the cement that was used to hold it in place. However, due to the small sample dimension and the very effective heater we consider this unlikely.

Once the dehydration front has passed, the porosity consolidates rapidly and does not change significantly anymore. The cumulative pore size frequency distribution over time (Figure 8) shows that, upon the initiation of dehydration, pores rapidly merge into a single cluster of interconnected pores (Figure 9, Suppl. Figure 4). This cluster connects the advancing reaction front with the outer surface of the unconfined sample.

Hildyard et al. (2011) describe networks of reacted and partly reacted material. They interpret the networks to delineate 'large-scale fluid pathways' during the advance of a dehydration front. The porous plumes we observed in our data are potentially related to these structures. A notable difference is that the plumes in our experiment encompass much smaller volumes compared to the networks in Hildyard et al.'s experiment (several hundreds of  $\mu\text{m}$ , cf. their Figure 3b). However, we found no evidence that drainage in our sample is controlled by some sort of hierarchical porous network but rather by the interconnected pore cluster shown in Figure 9 and Suppl. Figure 4.

### **4.3 Data processing**

The automated segmentation of grey scale images to isolate pores from their matrix is a critical processing step in the quantitative analyses of microtomographic data. Histogram-based thresholding is a rather simple method (Kaestner et al., 2008) and algorithms that utilize higher order information are generally favoured (e.g. Porter and Wildenschild, 2010, Wang et al., 2011). However, the intrinsic complexity of tomographic data generated from metamorphic rocks (which is constituted by the very large number of objects, their complicated shapes and wide range of size distributions, as well as the complex relationship to other phases) often renders advanced, feature-based techniques too difficult to use and computationally very expensive. Binary thresholding is a computationally efficient alternative.

All our SR $\mu$ CT data suffer from an intrinsic discretization error, which arises from the use of cubic voxels to represent real objects (e.g. Arns et al., 2002). This error affects all volumetric analyses we conducted. We designed our shrinking/expansion experiment to assess the largest possible error resulting from discretization and emphasize that the error estimates provided are certainly exaggerated. We stress that the excellent coincidence of the determined porosities (24-25 %, Table 2) with the theoretically expected porosity (29 %, assuming no compaction) indicate that our approach and the thresholds we chose deliver very good first-order results.

## 5. Conclusions

The dehydration of polycrystalline gypsum is often considered a proxy for metamorphic devolatilisation. Current models for dehydration under drained conditions are based on indirect measurements and post-experimental assessment of experimental charges in 2D. We conducted an in-situ Synchrotron X-ray microtomography experiment to document the dehydration of a 2.3 mm diameter cylinder of polycrystalline gypsum to overcome these limitations. We use a novel routine to segment porosity from the tomographic time-series data. The routine is based on time-dependent changes to the grey value distribution amongst cubic voxels of 2.197  $\mu\text{m}^3$  that record the absorption of x-rays in the sample. Our workflow allows determining position, shape, volume and orientation of each individual pore and quantifying percolation over multiple scales.

We show that the dehydration initiates across a sharp dehydration front. The front slowly propagates inward from the margin of the unconfined cylinder over more than four hours. The slow advance of the front is strongly non-linear and can be fitted with a linear diffusion equation yielding a diffusivity of  $8,290 \times 10^{-11} \text{ m}^2\text{s}^{-1}$ . The dehydration front delimits an unreacted inner domain, where no resolvable porosity could be observed, from an outer domain where anisotropic pores form. The non-random orientation of these pores can be explained by a preexisting fabric in the sample. Behind the dehydration front, isolated pores rapidly link to a large interconnected cluster of pores that connects to the outside of the sample at all times, providing a tortuous drainage pathway. We interpret gypsum in the inner domain to be stabilized by increased pressures. These likely result from the thermal expansion of gypsum and locally increased pore fluid pressures. Across the dehydration front, gypsum breakdown is very efficient and most likely controlled by the orientation of the gypsum lattice with respect to the advancing front. Gypsum breakdown initiates steadily grain by grain. We combine our observations in a model, in which the

dehydration of polycrystalline gypsum is controlled by a feedback of pressure release and pore formation on the grain scale. In a companion paper (Karrech et al., in prep.), we develop a theory that describes the advance of the dehydration front based on the dissipative mechanisms involved.

## **Acknowledgments**

This work was supported by the Western Australian State Government through the Premier's Fellowship Program and the Western Australian Geothermal Centre of Excellence Program, and the Australian Synchrotron Research Program, funded by the Commonwealth of Australia under the Major National Research Facilities Program. Use of the Advanced Photon Source at Argonne National Laboratory was supported by the U. S. Department of Energy, Office of Science, Office of Basic Energy Sciences, under Contract No. DE-AC02-06CH11357. SLF acknowledges funding by NERC, grant NE/C002938/1, and by Spanish Ministerio de Ciencia e Innovación, grant RYC-2008-02067. CS acknowledges funding by the German Research Foundation under Grant No. SCHR 1262/1-1. We thank iVEC@UWA in Perth for use of their computing facilities. We thank S. Revets for making unpublished results available and K. Gessner, and R. Hough for help with data acquisition. Reviews by H. Milsch and F. Trippetta helped to improve the manuscript and are gratefully acknowledged.

## **6. References**

- Arns, C. H., Knackstedt, M.A. Val Pinczewski, W., Garnoczi, E.J.: Computation of linear elastic properties from microtomographic images: Methodology and agreement between theory and experiment, *Geophysics*, 67/5, 1396-1405, 2002.
- Ballirano, P. and Melis, E.: Thermal behaviour and kinetics of dehydration of gypsum in air from in situ real-time laboratory parallel-beam X-ray powder diffraction, *Phys. Chem. Min.* 36, 391-402, 2009.
- Banhart, J.: *Advanced Tomographic Methods in Materials Research and Engineering*, Oxford University Press, USA, 2008.
- Bezou, C., Nonat, A., Mutin, J.-C., Christensen, A.N., Lehmann, M.S.: Investigation of the crystal structure of  $\gamma$ -CaSO<sub>4</sub>, CaSO<sub>4</sub>·0.5 H<sub>2</sub>O, and CaSO<sub>4</sub>·0.6 H<sub>2</sub>O by powder diffraction methods, *J. Solid State Chem*, 117, 165-176, 1995.
- Charola, A.E., Pühringer, J., Steiger, M.: Gypsum: a review of its role in the deterioration of building materials, *Environ Geol*, 52, 339-352, 2007.
- Christensen, A.N., Olesen, M., Cerenius, Y., Jensen, T.R.: Formation and Transformation of Five Different Phases in the CaSO<sub>4</sub>-H<sub>2</sub>O System: Crystal Structure of the Subhydrate  $\beta$ -CaSO<sub>4</sub> · 0.5H<sub>2</sub>O and Soluble Anhydrite CaSO<sub>4</sub>,

781 Chem. Mater. 20, 2124-2132, 2008.  
 782 Clauser, C. and Huenges, E.: Thermal conductivity of rocks and minerals, in: Rock  
 783 Physics and Phase Relations, A Handbook of Physical Constants, AGU  
 784 Reference Shelf 3, AGU, Washington, USA, 105 - 126, 1995.  
 785 Finot, E., Lesniewska, E., Mutin, J.-C., Goudonnet, J.-P.: Reactivity of gypsum faces  
 786 according to the relative humidity by scanning force microscopy, Surface  
 787 Science, 384, 201-217, 1997.  
 788 Freyer, D. and Voigt, W.: Crystallization and Phase Stability of  $\text{CaSO}_4$  and  $\text{CaSO}_4$ -  
 789 Based Salts, Monatsh. Chem. 134, 693-719, 2003.  
 790 Freyer, D. and Voigt, W.: Can mixtures of  $\alpha$ - and  $\beta$ -hemihydrates be quantified by  
 791 means of thermoanalysis? ZKG Int. 62, 3, 47-53, 2009.  
 792 Hacker, B.R.: Diagenesis and fault valve seismicity of crustal faults, JGR 102, B11,  
 793 24459-24467, 1997.  
 794 Heard, H.C. and Rubey, W.W.: Tectonic implications of gypsum dehydration, Geol.  
 795 Soc. Am.Bull., 77, 741-760, 1966.  
 796 Hildyard, R.C., Llana-Fúnez, S., Wheeler, J., Faulkner, D.R., Prior, D.J.: Electron  
 797 Backscatter Diffraction (EBSD) Analysis of Bassanite Transformation Textures  
 798 and Crystal Structure Produced from Experimentally Deformed and  
 799 Dehydrated Gypsum, J. Petrol., 52, 5, 839-856, 2011.  
 800 Jacques, S.D.M., González-Saborido, A., Leynaud, O., Bensted, J., Tyrer, M., Greaves,  
 801 R.I.P., Barnes, P.: Structural evolution during the dehydration of gypsum  
 802 materials, Min. Magaz. 73, 3, 421-432, 2009.  
 803 Kaestner, A., Lehmann, E., Stampanoni, M.: Imaging and image processing in  
 804 porous media research, Adv. Water Resour., 31, 1174-1187, 2008.  
 805 Karrech, A., Regenauer-Lieb, K., Schrank, C., Füsseis, F.: Dehydration of  
 806 polycrystalline gypsum, a theoretical and numerical investigation based on  
 807 first order thermodynamic principles, in prep.  
 808 Ko, S., Olgaard, D.L., Wong, T.-F., Generation and maintenance of pore pressure  
 809 excess in a dehydrating system 1. Experimental and microstructural  
 810 observations, JGR, 102, B1, 825-839, 1997.  
 811 Launeau, P., Archanjo, C.J., Picard, D., Arbaret, L., Robin, P.-Y.: Two- and three-  
 812 dimensional shape fabric analysis by the intercept method in grey levels,  
 813 Tectonophysics, 492, 230-239, 2010.  
 814 Liu, J., Regenauer-Lieb, K., Hines, C., Liu, K., Gaede, O., Squelch, A.: Improved  
 815 estimates of percolation and anisotropic permeability from 3-D X-ray  
 816 microtomography using stochastic analyses and visualization, Geochem.  
 817 Geophys. Geosy., 10, 5, doi: 10.1029/2008GC002358, 2009.  
 818 Liu, J., Regenauer-Lieb, K.: Application of percolation theory to  
 819 microtomography of structured media: Percolation threshold, critical

820 exponents, and upscaling, *Phys. Rev. E*, 83, 016106, 2011.

821 Llana-Fúnez, S., Brodie, K.H., Rutter, E.H., Arkwright, J.C.: Experimental  
822 dehydration kinetics of serpentinite using pore volumetry, *J. metamorphic*  
823 *Geol.*, 25, 423-438, 2007.

824 Llana-Fúnez, S., Wheeler, J., Faulkner, D.R.: The influence of confining pressure  
825 during metamorphism: dehydration experiments with gypsum, *Contrib.*  
826 *Mineral. Petr.*, submitted.

827 McConnel, J.D.C., Astill, D.M., Hall, P.L.: The pressure dependence of the  
828 dehydration reaction of gypsum, *Mineral. Mag.* 51, 453-457, 197.

829 Miller, S.A., van der Zee, W., Olgaard, D.L., Connolly, J.A.D.: A fluid-pressure  
830 feedback model of dehydration reactions: experiments, modeling, and  
831 application to subduction zones, *Tectonophysics* 370, 241-251, 2003.

832 Milsch, H.H. and Scholz, C.H.: Dehydration-induced weakening and fault slip in  
833 gypsum: Implications for the faulting process at intermediate depth in  
834 subduction zones, *J. Geoph. Res* 110, B04202, doi:10.1029/2004JB003324,  
835 2005.

836 Murrell, S.A.F. and Ismail, I.A.H.: The effect of decomposition of hydrous minerals  
837 on the mechanical properties of rocks at high pressures and temperatures,  
838 *Tectonophysics* 31, 207-258, 1976.

839 Olgaard, D.L., Ko, S., Wong, T.-F.: Deformation and pore pressure in dehydrating  
840 gypsum under transiently drained conditions, *Tectonophysics* 245, 237-248,  
841 1995.

842 Regenauer-Lieb, K. and Yuen, D.: Positive feedback of interacting ductile faults  
843 from coupling of equation of state, rheology and thermal-mechanics, *PEPI*,  
844 142, 113-135, 2004.

845 Schmidt, H., Paschke, I., Freyer, D., Voigt, W.: Water Channel Structure of  
846 Bassanite at High Air Humidity: Crystal Structure of  $\text{CaSO}_4 \cdot 0.625\text{H}_2\text{O}$ , *Acta*  
847 *Crystl B* 67, 467-475, with corrigendum in B68, 2011.

848 Singh, N.B. and Middendorf, B.: Calcium sulphate hemihydrate hydration leading  
849 to gypsum crystallization, *Prog. Cryst. Growth Ch.*, 53, 57-77, 2007.

850 Stauffer, D. and Aharony, A.: Introduction to Percolation Theory (2<sup>nd</sup> edition),  
851 Taylor & Francis Ltd., London, 1994.

852 Sprunt, E.S. and Brace, W.F.: Direct Observation of Microcavities in Crystalline  
853 Rocks, *Int. J. Rock Mech. Min. Sci. & Geomech. Abstr.* 11, 139 -150, 1974.

854 Stock, S.R.: Microcomputed Tomography, Methodology and Applications, Taylor  
855 & Francis Ltd, London, 2009.

856 Stretton, I.C.: An experimental investigation of the deformation properties of  
857 gypsum, PhD thesis, Univ. Manchester, 1996.

858 Wang, W.-H. and Wong, T.-F.: Effects of reaction kinetics and fluid drainage on

the development of pore pressure excess in a dehydrating system,  
Tectonophysics 370, 227-239, 2003.

Wang, W., Kravchenko, A.N., Smucker, A.J.M., Rivers, M.L.: Comparison of image  
segmentation methods in simulated 2D and 3D microtomographic images of  
soil aggregates, Geoderma, 162, 231-241, 2011.

## **Tables**

**Table 1** – Grain size and anisotropy characterization of the sample material.

**Table 2** – Porosities, total number of pores, the volume of the largest and second  
largest pore in the parallelepiped at different times during the experiment. See  
text for discussion.

**Figure captions**

**Figure 1** – To-scale sketch of the experimental set-up used within the X-ray beam configuration.

**Figure 2** – Vertical cross section through the sample at different times during the experiment (depicted in the four quadrants). The grey values correspond to the absorption of x-rays, pores appear dark grey to black. The white stippled frame outlines the location of the parallelepiped in which porosity was quantified (see text and also Suppl. Figure 5).

**Figure 3** – Histograms of the grey value distributions amongst the  $180 \times 10^6$  voxel constituting the parallelepiped in which porosity was quantified, at different times during the experiment. The vertical stippled line indicates the critical threshold we used for segmenting porosity.

**Figure 4** – Distribution of porosity along a radius at 10, 70 and 130 minutes. Note the slightly increasing background porosity in the inner domain. Values exceeding 30 % porosity result from the comparatively small sampling volume used to determine the porosity values shown.

**Figure 5** – The advance of the dehydration front, a) the position of the dehydration front in a horizontal section through the sample at different times during the experiment; b) the slow, highly non-linear radial progress of the front over time quantified from horizontal and vertical sections through the sample. See text for explanation of the technique. c) rose plot of linear diffusion constants derived from fitting Eq. 1 to propagation of dehydration front along radii in two horizontal cross sections through the sample. The higher diffusion coefficients probably relate to a pre-existing alignment of gypsum in part of the sample, as discussed in the text. Measurement strategy is explained in text (compare Suppl. Figure 3).

**Figure 6** – Porosity quantification in the parallelepiped outlined in Figure 2 and Suppl. Figure 5; a) Total porosity over time. Grey squares are the porosity values we determined using the threshold value derived from changes in the grey value histograms (Figure 3). The values correspond agreeably well with the theoretically predicted 30%. White and black squares, respectively, are the largest possible errors based on the numerical expansion/shrinking experiment, which is explained in the text. b) Total number of pores over time. Note that the value consolidates as soon as the dehydration front has propagated through the



sampling volume (after 130 min). White and black squares, respectively, are the largest possible errors derived from the numerical expansion/shrinking experiment. See text for further explanation.

**Figure 7** – Absolute pore size frequency distribution over time. The distribution consolidates as soon as the dehydration front has passed through the sampling volume (after 130 min).

**Figure 8** – Cumulative porosity size frequency distribution over time. The distribution is dominated by a single cluster of interconnected pores that makes up more than 90 per cent of the total porosity.

**Figure 9** – Horizontal section through the sample cylinder illustrating the largest interconnected pore cluster (in yellow) at different times during the experiment. Each quadrant shows the extent of the cluster at the time given by the number, the stippled line indicates the extent of the cluster 60 minutes earlier (in red). The sample diameter is 2.3 mm. The white frame indicates the location of the parallelepiped in which porosity was quantified.

**Figure 10** – Isotropy index over size of all pores [50; 450 voxel], [110; 989  $\mu\text{m}^3$ ] after 130 (left) and 310 minutes (right). Color-coded contours indicate data point density in per cent (calculated for moving search windows of size 50 voxel x 0.01 isotropy index units for a step size of 1 voxel in horizontal direction and 0.005 isotropy index units in vertical direction). Note that all pores are clearly anisotropic ( $I_i < 1$ ) in shape with most pores having indices between 0.2 and 0.4. This trend does not change with time.

**Figure 11** – Stereo plots showing the orientations of the longest principal axis of pores of different sizes. a) Orientations prior to heating, contours calculated from pores between 51 and 300 voxel, circles denote pores between 51 and 300 voxel in volume; b) Orientations after 70 minutes, contours are calculated from pores between 51 and 150 voxel, black circles are orientations of pores between 151 and 300 voxel and green circles of pores between 301-450 voxel; and c) Orientations after 310 minutes, contours are calculated from pores between 51 and 150 voxel, black circles are orientations of pores between 151 and 300 voxel and orange circles of pores between 301-450 voxel. The plots indicate that a pre-existing anisotropy controls the orientation of pores before and during dehydration.

**Figure 12** – Porosity frequency distribution amongst cubes with a 50-voxel side length sampled throughout the parallelepiped at different times during the experiment (see text for explanation). The shapes of the peaks give an indication of how homogeneously porosity is distributed within the sample, with the vertical lines marking the total porosity measured at different times. After 130 minutes the porosity distribution within the parallelepiped is relatively homogeneous.

**Figure 13** – Probability functions for percolation in the three principal directions amongst cubes with a 50-voxel side length placed in the parallelepiped. Each of the four diagrams compares two consecutive time steps. Dotted lines – x-axis, stippled line, y-axis, solid line – z-axis. Note that from 130 minutes onward, all cubes with more than about 22 % porosity are percolating in all three directions. In all cubes with a smaller porosity, the x-direction is most likely to percolate.

**Figure 14** – Sketch map illustrating the grain-by-grain advance of the dehydration front and the effect of the strong crystallographic anisotropy of gypsum. See text for discussion.

**Suppl. Figure 1** – Left: Photographs of thin sections of Volterra alabaster in polarized light with crossed polarizers. Right: Shape-fabric ellipsoids calculated with the line-intercept code by Launeau et al. (2010). Step size of rotation angle is  $10^\circ$ ; normal distance between search grid lines is 5 pixel. The largest mean grain size in the orientation interval  $[0^\circ; 360^\circ]$  is denoted by  $a$  (long axis of the fabric ellipsoid) while the smallest mean grain size is  $b$  (short axis of the fabric ellipsoid).  $R$  is the aspect ratio of the ellipsoid. The fabric ellipsoids show that Volterra gypsum exhibits a shape-preferred orientation locally.

**Suppl. Figure 2** – Temperature-Time curve of the experiment. Note that the tomographic data were acquired at 325 K after each heating period.

**Suppl. Figure 3** - Measurement strategy for the progress of the dehydration front over time from horizontal (upper panel) and vertical (lower panel) tomography slices. The global coordinate system is indicated on the right-hand side of the figure. Measurements of front position over time (as described in the text) are performed with a simple image analysis routine on binary images. The binary images are produced from the tomography data to segment unreacted from reacted material. The outer margin of the sample is easily separated from

the background (not shown; compare Fig. 2) by binary thresholding (accuracy is +/- 1 pixel). The position of the front at a given time, however, is determined by manual digitization. We estimate that the accuracy of this procedure is +/- 3 pixel (i.e., < 5  $\mu\text{m}$ ).

**Suppl. Figure 4** - Plot of proportions of sample area where reaction has initiated for two horizontal tomography slices (A and B) as a function of time. Note that in slice A the reaction initiation front has reached the centre of the cylinder before the last scan. Black solid line denotes calculation of reaction initiation progress assuming a perfectly concentric front propagation and the diffusivity determined with equation 1 (compare Fig. 5).

**Suppl. Figure 5** - Three-dimensional visualization of the morphology of the largest interconnected pore cluster at the reaction front - requires red-cyan glasses. Note the complexity of the pore shape. Side length of the cube shown is 200 voxel (260  $\mu\text{m}$ ).